

1 **Holocene sea ice and paleoenvironment conditions in the**
2 **Beaufort Sea (Canadian Arctic) reconstructed with lipid**
3 **biomarkers**

4 Madeleine Santos^{1,2}, Lisa Bröder¹, Matt O'Regan^{3,4}, Iván Hernández-Almeida^{1,5}, Tommaso Tesi⁶,
5 Lukas Bigler^{1,7}, Negar Haghipour^{1,8}, Daniel B. Nelson², Michael Fritz⁹, Julie Lattaud^{1,2,7}

6 ¹Department of Earth and Planetary Sciences, ETHZ, Zurich, 8092 Switzerland

7 ²Department of Environmental Science, University of Basel, Basel, 4056, Switzerland

8 ³Department of Geological Sciences, Stockholm University, Stockholm, 106 91, Sweden

9 ⁴Bolin Centre for Climate Research, – Stockholm University, Stockholm, 106 91, Sweden

10 ⁵Past Global Changes, University of Bern, Bern, 3012, Switzerland

11 ⁶Institute of Polar Sciences (ISP), Bologna, 40129, Bologna 40128, Italy

12 ⁷Department of Environmental Science, Stockholm University, Stockholm, 106 91, Sweden

13 ⁸Laboratory of Ion Beam Physics, ETHZ, Zurich, 8092, Switzerland

14 ⁹Alfred Wegener Institute, Helmholtz Centre for Polar and Marine Research, Potsdam, 14473, Germany

15

16 *Correspondence to:* Julie Lattaud (Julie.lattaud@aces.su.se)

17 **Abstract** The Beaufort Sea region in the Canadian Arctic has undergone substantial sea ice loss in recent decades,
18 primarily driven by anthropogenic climate warming. To place these changes within the context of natural climate
19 variability, Holocene sea ice evolution and environmental conditions (sea surface temperature, salinity, terrestrial
20 input) were reconstructed using lipid biomarkers (HBIs including IP₂₅, OH-GDGT, brGDGT, C_{16:0} fatty acid,
21 phytosterols) from two marine sediment cores collected from the Beaufort Shelf and slope, spanning the past 9.1 ka
22 and 13.3 cal. kyr BP, respectively. The Early Holocene (11.7–8.2 ka) is characterized by relatively higher sea surface
23 temperature, lower salinity and no spring/summer sea ice until 8.5 ka on the Beaufort Sea slope. Around 8.5 ka, a peak
24 in organic matter content is linked to both increased terrestrial input and primary production and may indicate
25 increased riverine input from the Mackenzie River and terrestrial matter input from coastal erosion. Following this
26 period, terrestrial inputs decreased throughout the **Mid-Holocene** in both cores. A gradual increase in IP₂₅ and HBI-II
27 concentrations aligns with relatively higher salinity, lower sea surface temperature and rising sea levels, and indicate
28 the establishment of seasonal (spring) sea ice on the outer shelf around 7 ka and on the shelf around 5 ka. These
29 patterns suggest an expansion of the sea ice cover beginning in the **Mid-Holocene**, influenced by decreasing summer
30 insolation. During the Late Holocene (4.2–1 ka), permanent sea ice conditions are inferred on the slope with a peak
31 during the Little Ice Age. After 1 ka, seasonal sea ice conditions on the slope are observed again, alongside an increase
32 in salinity and terrestrial input, and variable primary productivity. Similar patterns of Holocene sea ice variability have
33 been observed across other Arctic marginal seas, highlighting a consistent response to external climate forcing.
34 Continued warming may drive the Beaufort Sea toward predominantly ice-free conditions, resembling those inferred
35 for the Early Holocene.

36

37 **1. Introduction**

38 Sea ice is a critical component of the Arctic climate system, influencing ocean–atmosphere interactions, modulating
39 surface albedo (Kashiwase et al., 2017), regulating heat fluxes (Lake, 1967), and influencing ecosystem structure
40 through its control on light penetration and nutrient cycling (Lannuzel et al., 2020). Its high sensitivity to temperature
41 makes it both a driver and indicator of Arctic climate change. Since the late 1970s, satellite observations have revealed
42 a significant decline in Arctic sea ice extent, sparking interest in the mechanisms that govern sea ice variability over
43 multiple timescales (Stroeve et al., 2012). The Canadian Beaufort Sea is a marginal sea of the western Arctic Ocean
44 which exhibits strong seasonal and interannual variability in sea ice cover. Characterized by landfast ice on the shelf
45 and mobile pack ice offshore, this region has experienced significant sea-ice loss in recent decades due to rising
46 atmospheric and oceanic temperatures (Carmack et al., 2015; Comiso et al., 2008).

47 Understanding natural variability of sea-ice prior to the industrial era is critical for contextualizing recent trends.
48 Throughout the Holocene, Arctic sea ice has responded to changes in orbital forcing, ocean circulation, and ice sheet
49 dynamics (Park et al., 2018; Stein et al., 2017). During the **Late glacial**, abrupt climatic events such as Bølling-
50 Allerød (~14 – 12.8 ka) and Younger Dryas (~12.8–11.7 ka), contributed to the instability of the Arctic cryosphere.
51 In the Canadian Arctic, enhanced meltwater discharge and re-routing following the retreat of the Laurentide Ice
52 Sheet (LIS) contributed to oceanographic shifts and transient cooling events (Broecker et al., 1989). Lipid biomarker
53 records and climate simulations from the Arctic suggest reduced sea ice during the Early Holocene thermal
54 maximum (11–6 ka in the Canadian Arctic) (Kaufman et al., 2004), followed by expansion through the Middle to
55 Late Holocene, consistent with declining summer insolation (Stranne et al., 2014; Wu et al., 2020). Numerous
56 studies on Arctic sea ice variability have focused on offshore locations highlighting heterogeneity in sea-ice cover
57 history and the importance of local currents (Belt et al., 2010; Detlef et al., 2023; Fahl & Stein, 2012; Hörner et al.,
58 2016, 2018; Stein et al., 2017; Stein & Fahl, 2012; Vare et al., 2009; J. Wu et al., 2020). However, these studies
59 often neglected the spatial extent of sea ice cover toward the coast and the migration of the marginal ice zone.

60 Sea-ice cover can be reconstructed from microfossil and lipid biomarker evidence preserved in marine sediments.
61 Remains of sea-ice organisms such as dinocysts (de Vernal et al., 2013) and diatoms, the latter producing a specific
62 biomarker known as IP₂₅ (Belt et al., 2007), provide valuable records of past sea-ice conditions. This highly
63 branched isoprenoid (HBI) and its isomer HBI diene (HBI-II) are used to trace the presence of spring sea-ice in

64 modern and geological settings (e.g., Belt et al., 2010; Fahl & Stein, 2012; Hörner et al., 2016, 2018; Vare et al.,
65 2009). However, because the absence of these two HBIs may reflect either a permanent sea-ice condition (due to the
66 absence of light) or completely sea-ice free waters, the PIP₂₅ ratio was developed (Müller et al., 2011). This ratio
67 includes a phytoplankton biomarker (typically dinosterol, brassicasterol or HBI-III) that represents open-water
68 productivity. PIP₂₅ values have been used to distinguish between seasonal sea-ice (>0.5) and permanent sea-ice
69 cover (>0.75).

70 Sea-ice cover is influenced by both the atmospheric and the oceanic forcing, including salinity and temperature,
71 parameters that are often difficult to reconstruct in polar regions. Lipid biomarker and their (isotopic) ratios are a
72 useful toolkit for this purpose. In particular, compound-specific hydrogen isotopes of phytoplankton biomarkers
73 have shown promise for reconstructing past salinity (e.g., Lattaud et al., 2019; Sachs et al., 2018; Weiss et al., 2019).
74 However, in the Arctic Ocean, the generally low abundances of lipid biomarker restrict this approach to the
75 dominant lipid biomarkers, such as palmitic acid (C_{16:0} fatty acid, Sachs et al., 2018). In contrast to salinity, several
76 established proxies exist for reconstructing seawater temperature, including microfossil assemblages (e.g., dinocyst,
77 Richerol et al., 2008), inorganic ratios (e.g., Mg/Ca of foraminifera, Barrientos et al., 2018; Kristjánsdóttir et al.,
78 2007) and lipid biomarkers (Ruan et al., 2017; Varma et al., 2024). Among lipid biomarker proxies for cold water (<
79 15°C) environments, hydroxylated glycerol dialkyl glycerol tetraether (OH-GDGT) are particularly useful, with RI-
80 OH' and TEX-OH identified as promising seawater temperature indices (Lü et al., 2015; Varma et al., 2024).
81 Nevertheless, even the latest calibrations (Varma et al., 2024) reveal substantial uncertainty at low temperatures,
82 partly due to the limited representation of polar core-top sediments, which are biased toward the European and
83 Russian Arctic. These limitations highlight the need to further develop and test Arctic-specific proxies for both
84 salinity and seawater temperature.

85 This study presents a multi-proxy reconstruction of Holocene sea ice and oceanographic variability from two
86 sediment cores (PCB09, PCB11) collected from the Beaufort outer shelf and shelf slope. Lipid biomarkers,
87 including highly branched isoprenoids (HBIs), glycerol dialkyl glycerol tetraethers (GDGTs), the hydrogen isotopic
88 compositions of algal-derived fatty acids and terrestrial sterols, are used to reconstruct sea-ice cover, sea surface
89 temperatures (SSTs), salinity and terrestrial organic matter input. Additionally, a set of surface sediments is used to
90 assess the applicability and calibrate salinity and SST proxies in sediments of the Beaufort Sea.

91 The primary objectives are to (1) reconstruct past variations in sea-ice cover on the Beaufort Shelf throughout the
92 Holocene, (2) explore the potential roles of insolation changes, meltwater input, and oceanic conditions in shaping
93 regional sea-ice variability, and (3) place the Beaufort Sea record within a broader Arctic context to provide insights
94 into past and present climate variability.

95 **2. Materials and Methods**

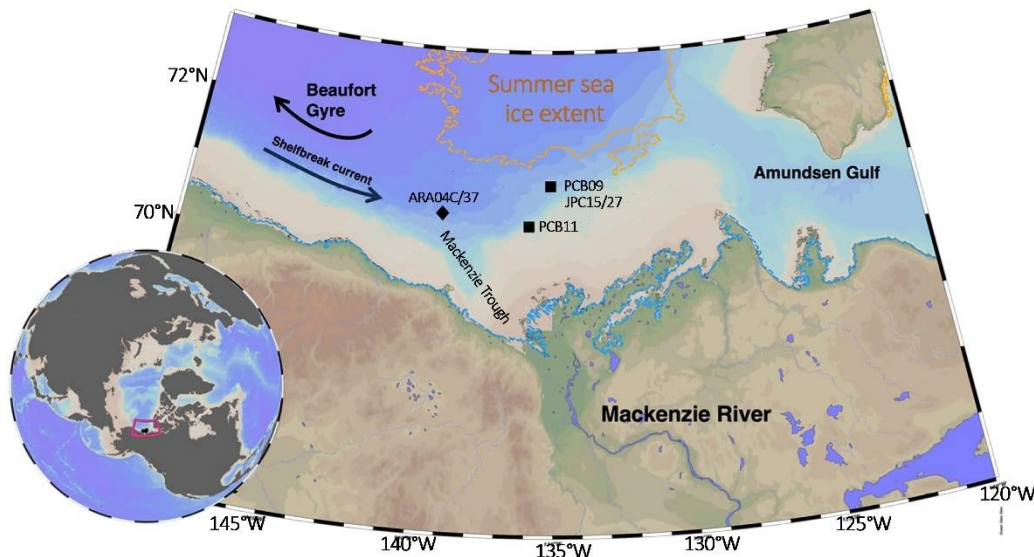
96 **2.1. Study area**

97 The study focuses on the Canadian Beaufort Sea, one of the marginal seas of the Arctic Ocean (Fig. 1), bounded by
98 the glacially excavated Amundsen Gulf to the east, Mackenzie Trough to the west, and the Mackenzie River delta to
99 the south (Carmack et al., 2004). The shelf is a large estuarine setting at the interface between the Arctic Ocean and
100 the Mackenzie River (Omstedt et al., 1994) (Fig.1). The Mackenzie River is a significant source of freshwater to the
101 Beaufort Sea, with an annual water discharge of $316 \text{ km}^3 \text{ yr}^{-1}$ (Holmes et al., 2012) and is considered the largest
102 Arctic river in terms of sediment flux ($124\text{--}128 \text{ Mt}\cdot\text{yr}^{-1}$) (Stein et al., 2004). At the same time, permafrost coastal
103 erosion adds another $8\text{--}9 \text{ Mt}\cdot\text{yr}^{-1}$ of sediment into the Beaufort Sea, including carbon and nutrients (Wegner et al.,
104 2015). Surface water circulation in the Beaufort Sea is primarily characterized by the clockwise Beaufort Gyre,
105 which drives offshore currents towards the west and traps the majority of the Arctic Ocean's freshwater in the
106 Canada Basin (Serreze et al., 2006). There is also a eastward flowing shelf-break current at depths beneath 50 m,
107 which transports Pacific Water (coming from the Bering Strait) along the slope (Pickart, 2004). Sea ice cover on the
108 Beaufort Shelf north of the Mackenzie River Delta varies from year to year, but generally begins to form in mid-
109 October, persisting until ice break up in April-May (Fig. S1). During ice break up, an open water flaw lead occurs
110 along the outer edge of the landfast ice establishing a spring marginal ice zone over the shelf.

111 **2.2. Material**

112 Two sediment cores were analyzed in the study. They were recovered as part of the Permafrost Carbon on the
113 Beaufort Shelf (*PeCaBeau*) project during the 4th Leg of the 2021 CCGS Amundsen expedition (Bröder et al., 2022,
114 Fig.1). At station PCB09 (71.1°N , 135.1°W) at a water depth of 675 m on the Beaufort shelf slope, a piston core
115 (PC, length of 420 cm) and multicore (MC, 30 cm) were retrieved (Fig. 1). At station PCB11 (70.6°N , 136.0°W) on
116 the outer Beaufort shelf (74 m water depth) a giant gravity core (GGC, length of 290 cm) and MC (32 cm) were

117 recovered (Fig. 1). PCB09 is found within the modern Atlantic bottom water mass, while PCB11 lies within the
118 Pacific summer water (Fig. S2), the water masses were defined as in Matsuoka et al. (2012). The core tops (0-1cm)
119 from 22 multicores collected during *PeCaBeau*, were used to ground truth the hydrogen isotope ratio of C_{16:0} fatty
120 acid proxy for reconstructing salinity and test the applicability of the **SST** reconstructions (Fig. S1).



121
122 Figure 1: Combined topographic and bathymetric map of the Beaufort Shelf region (Canadian Arctic) displaying the
123 cores from this study as black squares (PCB09 and PCB11) and key records discussed in the text (ARA04C/37 from
124 Wu et al., 2020; JPC15/27 from Keigwin et al., 2018). The 2021 summer sea-ice extent is outlined by the orange
125 dotted line, the winter sea ice extent follows the coastline (Meier et al., 2018). Map generated using Ocean Data View
126 (Schlitzer, 2025).

127 **2.3. Methods**

128 **2.3.1. Core processing**

129 During the PeCaBeau expedition, all cores were scanned shipboard on a Geotek multi-sensor core logger (MSCL).
130 Bulk density and magnetic susceptibility were measured at a 1 cm downcore resolution on the piston and gravity cores,
131 (Bröder et al., 2022). The cores remained unopened and were shipped to AWI Potsdam following the expedition. They
132 were subsequently split in the fall/winter and the working halves sampled using 2x2 cm u-channels, before being cut
133 into 1-2 cm thick slices which were frozen and freeze dried.

134 An ITRAX XRF-core scanner was used to measure relative elemental abundances at Stockholm University, Sweden.
135 Measurements were performed on u-channel samples at a downcore resolution of 2 mm. Analyses were made using a
136 Mo tube at a voltage of 55 kV, a current of 50 mA and an exposure time of 20 s. Here we present the ratios of Ca/Ti,

137 reflecting detrital carbon inputs regionally elevated by meltwater delivery from either the Mackenzie or Amundsen
138 Gulf during deglaciation (Klotzko et al., 2019; Swärd et al., 2022; J. Wu et al., 2020). Zr/Rb was used as a proxy for
139 grain size variations as Zr content is elevated in coarse minerals, while Rb is associated with clay minerals (L. Wu et
140 al., 2020) and Br/Cl as a proxy for marine organic matter as Br usually correlates well with OC content (Wang et al.,
141 2019).

142 **2.3.2. Age model**

143 The chronology of the piston and gravity cores (Fig. 2) were determined by ^{14}C dating of foraminifera (n = 13,
144 PCB09) and bivalve shells (n = 7, PCB11) (Table S1). The MSCL data was used to stratigraphically correlate
145 PCB09 with JPC15/27 (Keigwin et al., 2018) allowing us to integrate existing radiocarbon ages (n=8) from this
146 record with our new data (n=5) (Fig. S3).

147 Bivalve shells were either picked from the split cores when sampling, or later from the freeze-dried sediments.
148 Foraminifera were picked from the $>45\text{ }\mu\text{m}$ fraction of the wet-sieved samples following organic extractions.
149 Foraminifera samples consisted of either planktonic (*Neogloboquadrina pachyderma*), benthic, or a combination of
150 both in horizons when specimens were extremely rare. Care was given to pick well preserved foraminifera to avoid
151 age bias (Wollenburg et al., 2023). Foraminifera and mollusk samples were prepared for Accelerator Mass
152 Spectrometry (AMS) analyses at the Laboratory for Ion Beam Physics at ETHZ using procedures described in
153 (Missiaen et al., 2020) which include sieving and acid cleaning to remove impurities from the shells.

154 Radiocarbon-based age models were generated using the BACON package in R (Blaauw & Christen, 2011) and the
155 Marine20 calibration curve (Heaton et al., 2020). A reservoir age of 330 ± 41 years was applied to the Holocene-age
156 mollusc samples in PCB11 as determined by West et al. (2022) for Pacific waters entering the Arctic Ocean in the
157 Chukchi Sea. For PCB09 we applied the approach used for JPC15/27 (Keigwin et al., 2018) and for ARA04C/37 (J.
158 Wu et al., 2020) but updated for Marine20 as described by Lin et al. (2025). A reservoir correction of -150 ± 100
159 years was applied to Holocene planktic foraminifera, and a larger reservoir correction (50 ± 100 years) for the
160 bottom 4 samples (Table S1) that fall within the Younger Dryas. In our age model we also incorporate samples of
161 benthic foraminifera that were calibrated using a reservoir correction of 206 ± 67 years, determined by (West et al.,

162 2022) for Atlantic waters near the Chukchi Sea. Samples containing mixed planktic and benthic foraminifera were
163 calibrated using an average of these values (28 ± 85 years).

164 **2.3.3. Bulk organic matter**

165 For the determination of total organic carbon (TOC) content and stable carbon isotope composition ($\delta^{13}\text{C}$) at the
166 University of Basel, about 12 mg of freeze-dried sediment was weighed into each silver capsule and 1-2 drops of
167 distilled water were added. The samples were exposed to fuming hydrochloric acid (HCl, 37%) in a desiccator for
168 24 hours to remove inorganic carbon. Samples were dried (48 h, 50 °C) and analyzed using an elemental analyser
169 coupled to an isotope mass spectrometer (Sercon, Integra 2). The standards used to calculate TOC was
170 Ethylenediaminetetraacetic acid (EDTA, Sigma Aldrich) and for $\delta^{13}\text{C}$ were USGS40 ($-26.389 \pm 0.042\text{\textperthousand}$, IAEA),
171 USGS64 (-40.81 ± 0.04 , IAEA), and USGS65 (-20.29 ± 0.04 , IAEA). The analytical precision, defined as the standard
172 deviation of the measurement of the USGS standards for the $\delta^{13}\text{C}$ sequence was $\pm 0.03\text{\textperthousand}$.

173 **2.3.4. Lipid biomarkers**

174 Lipid biomarkers were analysed from 42 samples (every 10 cm for the first 143 cm, then every 20 cm) for PCB09
175 and 21 for PCB11 (every 20 cm). Core top samples from the MC's were also analysed for lipid biomarkers. For each
176 sample, 5 g of homogenized freeze-dried sediment was extracted using an Energy Dispersive Guided Extraction
177 (EDGE) following (Lattaud, Bröder, et al., 2021). Briefly, after extraction with dichloromethane (DCM): methanol
178 (MeOH) (9:1, v/v), the total lipid extracts (TLE) were saponified at 70 °C for two hours (with KOH in MeOH at
179 0.5M). The neutral phase was collected by liquid-liquid extraction with 10 mL of hexane, three times. The leftover
180 TLE was acidified to pH 2 and the acid phase was recovered by liquid-liquid extraction adding 10 mL hexane:DCM
181 (4:1, v/v), three times. The acid compounds were methylated by adding MeOH:HCl (95:5, v/v) and heated at 70°C
182 overnight. The methylated fatty acids were recovered by liquid-liquid extraction (three times) with 10 mL
183 hexane:DCM (4:1, v/v). Internal standards were added to the neutral fraction prior to silica chromatography: 7-
184 hexynonadecane (7-HND, provided by S. Belt), 9-octylheptadec-8-ene (9-OHD, provided by S. Belt), C₂₂ 5,16-diol
185 (Interbioscreen), C_{36:0} alkane (Sigma Aldrich) and C₄₆ GDGT-like compound(C₄₆ glycerol trialkyl glycerol
186 tetraether, GTGT, Huguet et al., 2006). The neutral phase was separated into three fractions (F1, F2, and F3) through

187 silica column (combusted and deactivated 1%) using hexane:DCM (9:1, v/v), DCM, and DCM: MeOH (1:1, v/v),
188 respectively.

189 The F1 containing HBIs was analyzed on a GC-MS (Agilent 7890-5977A) operating in Selective Ion Monitoring
190 (SIM) mode at the Institute of Polar Sciences (ISP), Bologna, Italy, following (Belt et al., 2014). The column used
191 was a J&W DB5-MS (length 30 m, id 250 μ m, 0.25 μ m thickness). Integrations were done in SIM mode for IP₂₅
192 (m/z = 350), HBI II (m/z = 348) and HBI III and HBI IV (m/z = 346). Concentrations of IP₂₅ were corrected for m/z
193 348 influence (4 %) and instrumental response factor. 9-OHD (m/z 350) was used to quantify HBIs. A reference
194 sediment containing known amount of IP₂₅ was run in parallel to correct IP₂₅ concentration.

195 F3 was split in two with one aliquot that was filtered using a polytetrafluoroethylene filter (PTFE, 0.45 μ m pore
196 size) and analyzed for GDGTs with high performance liquid chromatography (LC)/atmospheric pressure chemical
197 ionization-MS on an Agilent 1260 Infinity series LC-MS according to Hopmans et al. (2016) with the adaptation of
198 Lattaud, De Jonge, et al. (2021). GDGTs were quantified using the C₄₆ GTGT internal standard assuming the same
199 response factor.

200 The other F3 aliquot was silylated with bis(trimethylsilyl)trifluoroacetamid (BSTFA) (70 °C 30 min) and analysed at
201 the ISP for sterol concentration (brassicasterol, stigmasterol, β -sitosterol, campesterol) on a GC-MS. The C₂₂ 5,16-
202 diol is used to quantify sterols. Specific m/z ratios have been extracted from chromatograms in order to identify each
203 biomarker according to their respective mass spectra, sterols were quantified on the total ion current.

204 Lipid δ^2 H values were analyzed by GC coupled to an isotope ratio mass spectrometer (IRMS) on all acid fractions
205 having adequate compound abundance. Samples were analyzed using splitless injection with a split/splitless inlet at
206 280 °C and a Restek Rtx-5MS GC column (30 m \times 0.25 mm \times 0.25 μ m) with helium carrier gas at 1.4 mL min⁻¹. The
207 GC oven was held at 60°C for 1.5 min, ramped to 140°C at 15°C min⁻¹, then to 325 °C at 4 °C min⁻¹, and held for
208 15 min. Column effluent was pyrolyzed at 1420°C, and δ^2 H values were measured on a Thermo Delta V Plus IRMS.
209 The H₃⁺ factor was evaluated with each measurement sequence to confirm stability. Values were always lower than
210 3 ppm mV⁻¹. Reference standards with known isotopic compositions (Mix A7, USGS71, C_{30:0} FAME; provided by
211 Arndt Schimmelmann, Indiana University, USA) were analyzed alongside samples to normalize values to the
212 Vienna Standard Mean Ocean Water- Standard Light Antarctic Precipitation (VSMOW-SLAP) scale. Standards
213 were injected at a range of concentrations so that peak size effects could be assessed and corrected for. Quality
214 control samples with known δ^2 H values were measured as unknowns to check precision and accuracy (C_{16:0} FAME

215 in mix F8-40, C_{30:0} FAME; Arndt Shimmelmann), which were 4.2 ‰ or better, and 1.0 ‰ or better, respectively (n =
216 13-16). Final fatty acid δ²H values of C_{16:0} were corrected for added hydrogen during methylation following [Eq. 1].

217
$$\delta^2H_{C16:0} = \frac{(nH_{FAME} + nH_{CH_3}) \times \delta^2H_{FAME\ measured} - nH_{CH_3} \times \delta^2H_{CH_3}}{nH_{FAME}} \quad (1)$$

218 Where nH_{CH₃} = 3, nH_{FAME} = 32.

219 **2.3.5. Biomarker ratios and environmental indicator reconstructions (sea ice, salinity, SSTs)**

220 In order to describe sea ice variability in the Holocene, the PIP₂₅ index is used (Müller et al., 2011). The PIP₂₅ index
221 [Eq. 2] uses additional phytoplankton biomarkers (i.e. brassicasterol, dinosterol, and HBI-III) which indicate open
222 water conditions to compare with the abundance of IP₂₅ (Belt et al., 2007):

223
$$PIP_{25} = \frac{IP_{25}}{[IP_{25}] + [Phytoplankton\ biomarker]*c} \quad (2)$$

224 HBI-III was used in this study (Belt et al., 2015; Kolling et al., 2020; Köseoğlu et al., 2018; Smik et al., 2016) as a
225 reference for pelagic phytoplankton to derive P_{HBI}IP₂₅ index (afterward called PIP₂₅). Dinosterol was not detected in
226 the samples which is common in the Beaufort Sea (Fu et al., 2025), and brassicasterol has been shown to derive mainly
227 from terrestrial input in the region (J. Wu et al., 2020). The c value represents the ratio of the mean concentration of
228 IP₂₅ over the mean concentration of HBI-III of all samples for each core (4.79 for PCB09 and 5.55 for PCB11).

229 Surface salinity was reconstructed using the calibration between δ²H of C_{16:0} fatty acid (palmitic acid) and salinity
230 from the test study of Sachs et al. (2018) [Eq. 3], adding data from Allan et al. (2023) and after testing surface
231 sediments from multicores from the region (Fig. S4):

232
$$\delta^2H_{PA} = 4.22 (\pm 0.6) * S - 338 (\pm 15) \quad (3)$$

233 where S is salinity in practical salinity units (PSU). Based on the known calibration errors (4‰ for the δ²H
234 measurement), reconstructed salinity should have an associated error of ± 7 PSU.

235 To reconstruct SST, hydroxylated GDGTs (OH-GDGTs) were used as the hydroxyl group in these GDGTs is
236 suggested to be an adaptation feature to regulate permeability in cold waters (Liu et al., 2012). In this study, the RI-
237 OH' [Eq. 4] and TEX-OH [Eq. 5] indexes were calculated:

238
$$\text{RI-OH}' = \frac{[\text{OH-GDGT-1}]+2*[\text{OH-GDGT-2}]}{[\text{OH-GDGT-0}]+[\text{OH-GDGT-1}]+[\text{OH-GDGT-2}]} \quad (4)$$

239
$$\text{TEX - OH} = \frac{\text{GDGT-2+GDGT-3+Cren isomer}}{\text{GDGT-2+GDGT-3+Cren isomer+OH-GDGT-0+GDGT-1}} \quad (5)$$

240 For the conversion from RI-OH' and TEX-OH to SST, the recent calibration of Varma et al. (2024) is used [Eq. 6 and
241 7]:

242
$$\text{RI-OH}' = 0.04 \times \text{SST} + 0.003 \quad (6)$$

243
$$\text{TEX - OH} = 0.021 \times \text{SST} + 0.08 \quad (7)$$

244 Several organic proxies have been used to interpret terrestrial organic matter input such as branched glycerol dialkyl
245 glycerol tetraether (brGDGTs), long chain *n*-alkanes, and plant sterols. BrGDGTs are membrane lipids synthesized
246 by bacteria and are known to be ubiquitous in terrestrial environments (Schouten et al., 2013). The BIT index
247 (Hopmans et al., 2004) [Eq.8] is a common indicator of terrestrial input into the marine realm:

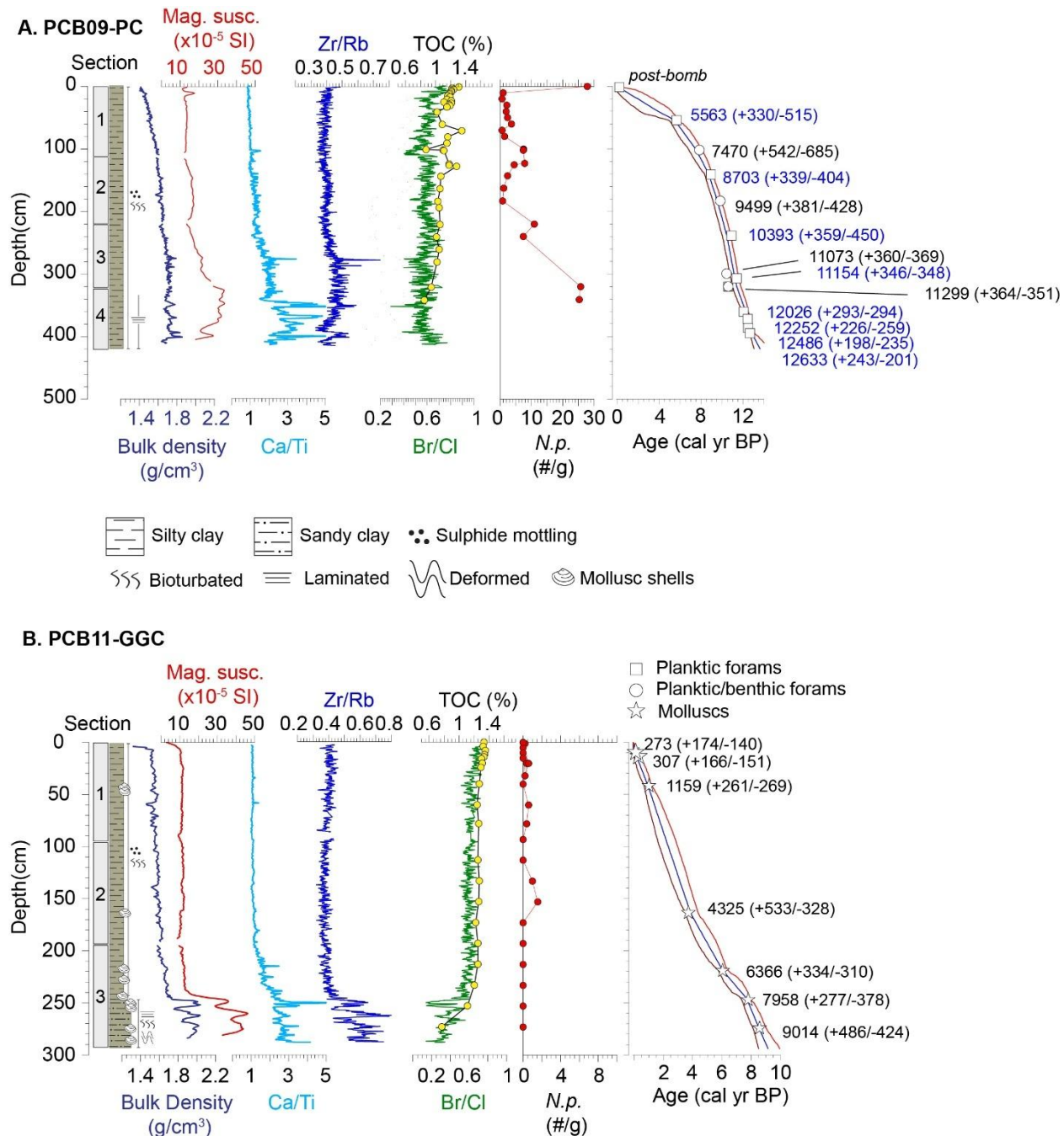
248
$$\text{BIT} = \frac{[\text{BrGDGT-}Ia+IIa+IIIa]}{[\text{BrGDGT-}Ia+IIa+IIIa]+\text{Crenarcheol}} \quad (8)$$

249 In addition, in situ marine production of brGDGT can occur in coastal sediments between 50 and 300 m water depth
250 (Peterse et al., 2009; Sinninghe Damst , 2016). To assess the potential for brGDGT to be produced in situ we
251 calculated the number of cyclopentane rings present in the tetraether brGDGT (#ring_{tetra}) [Eq 9]:

252
$$\#ring_{tetra} = \frac{(Ib+2\times Ic)}{(Ia+Ib+Ic)} \quad (9)$$

253 **2.3.6. Micropaleontology**

254 Extracted sediments were wet sieved using a 45 µm mesh. The >45 µm fraction was dried in the oven (40 °C) and
255 picked for foraminifera using a stereoscopic microscope. Planktonic foraminifera species are identified
256 (<https://www.mikrotax.org/pforams/>) using the morphological descriptions compiled in Microtax and counted for each
257 sample.



260 *Figure 2: Core description for (a) PCB09 and (b) PCB11 presenting lithostratigraphy, bulk density, magnetic*
 261 *susceptibility, X-Ray Fluorescence (XRF) results including Ca/Ti, Zr/Rb and Br/Cl ratios. Total organic carbon*
 262 *content (%) and abundance of *N. pachyderma* (N. p., number/gram of sediment) as well as the age models of PCB09*
 263 *and PCB11 generated using the Bacon Rpackage (Blaauw & Christen, 2011). The red bands illustrate the 95%*
 264 *confidence level around the modelled median age (blue line). Symbols indicate the calibrated age of the dated material*
 265 *before age-modelling. The errors on these are lower than the symbol size. The numbers are the median modelled ages*

266 and 95% error at the location of each sample. Blue radiocarbon ages originated from nearby core HLY13-15JPC
267 (Keigwin et al., 2018).

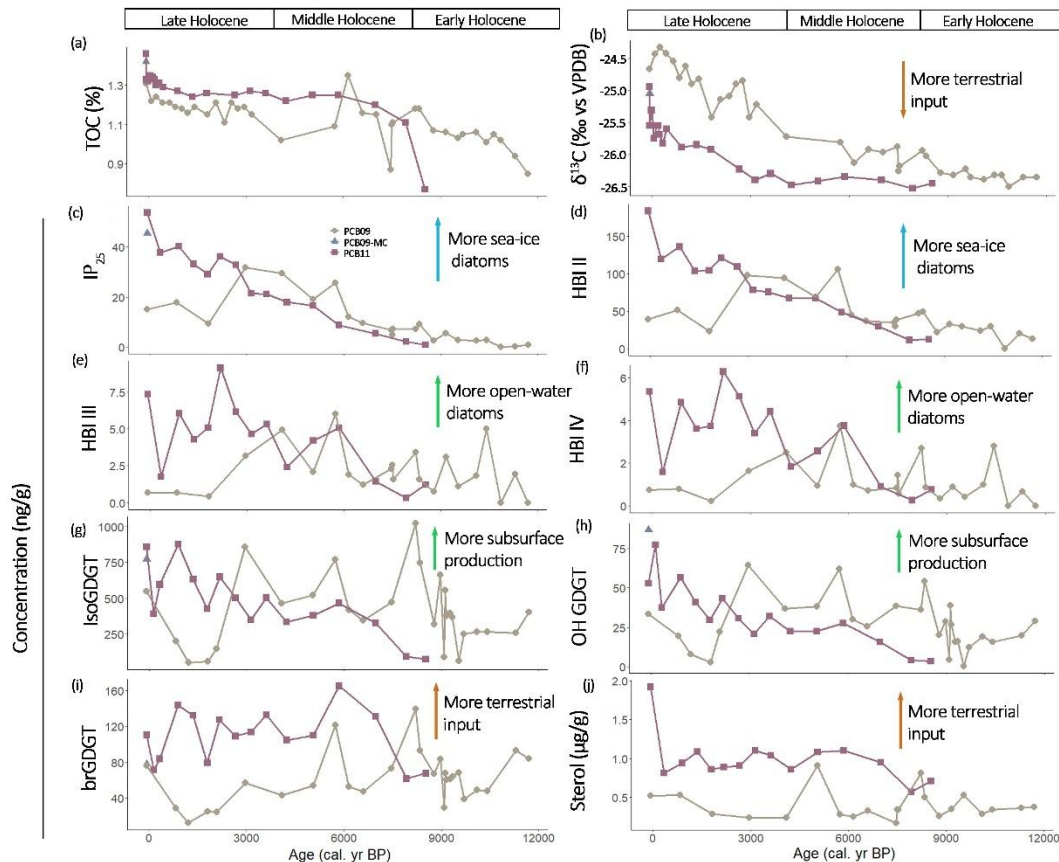
268 **3.1. Core chronology, lithostratigraphy and bulk organic matter**

269 The age models of cores PCB09 (Fig. 2a) and PCB11 (Fig. 2b) show that they cover the last 13350 ± 690 cal. yr BP
270 and 9120 ± 720 cal. yr BP, respectively. PCB11 had a mean sedimentation rate of 35 ± 10 cm kyr^{-1} with slightly
271 higher sedimentation rates in the Late Holocene (< 4 ka). Conversely, PCB09 had an average sedimentation rate of
272 50 ± 27 cm kyr^{-1} , with substantially higher sedimentation rates before the Late Holocene.

273 The upper 300 cm of PCB09 (0 – 11 ka) display a gradual downcore increase in bulk density, reflecting porosity loss
274 in largely homogenous silty-clay sediments (Fig 2a). Below 300 cm, slightly higher variability in the bulk density,
275 elevated magnetic susceptibility and higher Zr/Rb all point towards a transition to slightly coarser-grained sediments.
276 Ca/Ti tended to increase downcore becoming more variable below 105 cm (7.6 ± 0.6 cal yr BP). There was a notable
277 stepwise increase in Ca/Ti at 345 cm (11.7 ± 0.4 ka, Fig. 2a). Discrete peaks in Zr/Rb and bulk density, indicative of
278 sediment coarsening, co-occurred with elevated Ca/Ti ratios at depths of 276 cm (10.8 ± 0.4 cal. yr BP), 345-352 cm
279 (11.8 ± 0.4 cal. yr BP) and 402 cm (12.8 ± 0.4 cal. yr BP).

280 A similar pattern is seen in PCB11, where below 240 cm (7.4 ± 0.6 cal yr BP) there was an abrupt increase in bulk
281 density, magnetic susceptibility, Zr/Rb and Ca/Ti. TOC concentrations and the Br/Cl ratio (which mirrors small scale
282 changes in the TOC) also decreased notably through this interval (Fig. 2b, 3a). This lithologic transition post-dates
283 the **Late glacial** and Early Holocene detrital carbonate inputs in cores recovered from the Beaufort Sea slope (Klotsko
284 et al., 2019). It is likely that this coarser basal facies is related to the inundation of the shelf during transgression.

285 Bulk sediment $\delta^{13}\text{C}$ of PCB09 was lowest in the Early Holocene at approximately $-26.3\text{\textperthousand}$ until 8.7 ± 0.4 ka, before
286 increasing during the Middle and Late Holocene to $-24.7\text{\textperthousand}$ (Fig. 3b). The trend in $\delta^{13}\text{C}$ in PCB11 is similar to
287 PCB09 showing a steady increase over time from $-26.5\text{\textperthousand}$ to $-25.8\text{\textperthousand}$.



288

289 Figure 3: Bulk characteristics and biomarker concentrations (in ng/g sediment) for core PCB09 (brown circles) and
 290 PCB11 (red squares) with (a) total Organic Carbon (TOC), (b) $\delta^{13}\text{C}$, (c) IP₂₅, (d) HBI-II, (e) HBI III, (f) HBI IV, (g)
 291 isoprenoid GDGTs (isoGDGT), (h) hydroxylated GDGTs (OH-GDGT), (i) branched GDGTs (brGDGT) and (j)
 292 terrestrial sterols (sum of brassicasterol, stigmastanol, β -sitosterol, campesterol).

293 **3.2. Lipid biomarkers**

294 IP₂₅ and HBI II (C_{25:2}) concentrations were generally low (< 2 ng/g) in the Early Holocene (Fig. 3c,d). IP₂₅ in both
 295 cores increased throughout the Middle to Late Holocene. During the Late Holocene, IP₂₅ and HBI II concentrations
 296 dropped in PCB09 around 1.8 ± 1.5 ka. Concentrations of both biomarkers were higher in PCB11 than in PCB09
 297 after 3 ka, reaching modern values of 40 ng g⁻¹ and 150 ng g⁻¹ (IP₂₅ and HBI II). PIP₂₅ values in both cores increased
 298 from the Early to the Mid-Holocene (Fig. 4a).

299 HBI III (C_{25:3}) and HBI IV (C_{25:4}) were low in both cores with values below 8 ng g⁻¹ (Fig. 3e,f). Concentrations were
 300 higher in PCB11 than in PCB09 after 4 ka

301 The concentration of isoGDGTs and OH-GDGTs followed a similar pattern throughout the Holocene (Fig. 3g,h).
302 IsoGDGTs and OH-GDGT concentrations in PCB09 were stable during the Early Holocene at around 400 ng g⁻¹ and
303 25 ng g⁻¹, respectively. At around 8.5 ka, the isoGDGTs and OH-GDGT amounts doubled. Throughout the **Mid-**
304 **Holocene**, isoGDGTs and OH-GDGT concentrations were variable but above 500 ng g⁻¹. A drop in PCB09 to almost
305 below detection limits occurred between 1-1.5 ka. IsoGDGTs and OH-GDGTs in PCB11 showed a steady increase
306 from around 100 ng g⁻¹ and 10 ng g⁻¹, respectively, in the Early Holocene to >500 ng g⁻¹ and >50 ng g⁻¹ (Fig. 3g,h).

307 BrGDGTs concentrations in PCB09 were below 100 ng g⁻¹ throughout the cores except for peaks during the Early
308 and **Mid-Holocene** at 11.2 ± 0.3, 8.2 ± 0.5 and 5.7 ± 0.5 ka, the latter was also seen in PCB11 (albeit concentrations
309 were higher in PCB11) (Fig. 3i). BIT values varied from 0.1 to 0.4 in PCB09 and from 0.1 and 0.5 in PCB11. The
310 #ring_{tetra} values were always < 0.7 for both cores. Terrestrial sterol concentrations in PCB09 were relatively stable
311 throughout the core except for short-lived peaks at 9.5 ± 0.4, 8.2 ± 0.5 and 5.0 ± 0.9 ka (Fig. 3j). In PCB11, the
312 concentration remained stable throughout the core after an initial increase at 6.9 ± 0.6 ka and a peak in the surface
313 sediment.

314 Although biomarker concentrations expressed per gram of sediment may be influenced by mineral dilution or post-
315 depositional degradation, TOC contents in our cores varied only slightly (0.9-1.3 % in PCB09 and 1.1-1.3 % in
316 PCB11; Figure 3a). Such limited variability indicates that TOC normalization would not substantially alter the
317 observed trends. The distinct downcore patterns among lipid biomarker classes therefore likely reflect differences in
318 source input and preservation rather than a uniform effect of degradation or dilution.

319 **3.5. Salinity, SST and terrestrial input inferred from biomarker ratios**

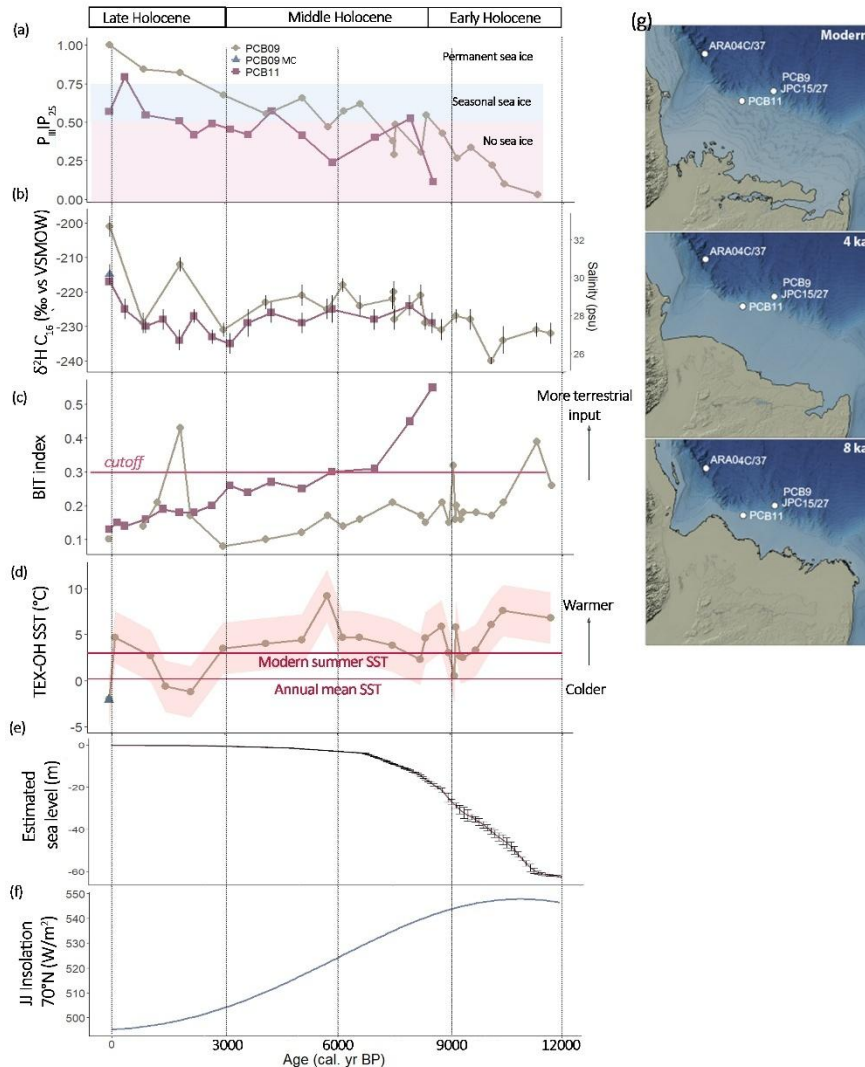
320 Surface sediments δ²H C_{16:0} values from the Beaufort Sea (Fig. S1, S4) range from -275 to -200‰, comparable with
321 the values obtained by the preliminary study of Sachs et al. (2018). δ²H C_{16:0} values of all sediments correlate with
322 summer salinity ($r^2 = 0.63$, $p < 0.001$) and the calibration equation is the same as the one obtained by Sachs et al.
323 (2018). It is to be noted that the uncertainty associated with the analysis and calibration reaches 7 psu, which is quite
324 large for salinity changes over glacial-deglacial timescales. This is to the contrary to what Allan et al. (2023) and J.
325 Wu et al. (2025) observed in a set of surface sediments in Baffin Bay and a downcore record of the Beaufort Sea,
326 where no relationship with salinity is observed. This contrast for the surface sediments could come from the different
327 environment as Baffin Bay is a much more enclosed basin compared to the Beaufort Sea, or that δ²H C_{16:0} values

328 encompassed a too small range of salinity (28 – 34 psu). The downcore Beaufort Sea record yielded no notable salinity
329 response of the $\delta^2\text{H}$ $\text{C}_{16:0}$ when large freshwater influence were expected, which was attributed to the production of
330 $\text{C}_{16:0}$ by heterotrophs (J. Wu et al., 2025).

331 Sea surface salinity inferred from $\delta^2\text{H}$ $\text{C}_{16:0}$ values at PCB09 increased from $27 \text{ psu} \pm 7$ during the Early Holocene to
332 $30 \pm 7 \text{ psu}$ during the **Mid-Holocene**, and remained stable until 3 ka, increasing to $32 \pm 7 \text{ psu}$ during the Late Holocene
333 (Fig. 4b). Reconstructed salinity at PCB11 was more stable during the **Mid-Holocene** and Late Holocene ($28 \pm 7 \text{ psu}$)
334 until an increase to $30 \pm 7 \text{ psu}$ in the last centuries. (Fig. 4b). Although uncertainties associated with reconstructed
335 salinity are large ($\pm 7 \text{ psu}$) the salinity trend between both locations agree with modern observations of lower salinities
336 at PCB11 than further offshore at PCB09 (Fig. S2).

337 Two different sets of SSTs were reconstructed using the OH-GDGT only (RI-OH') or a combination of OH- and
338 isoGDGT (TEX-OH) (Fig. 4d, Fig. S4, S5a,b). SSTs were only reconstructed when the BIT index was below 0.3 (Fig.
339 4c) as both calibrations are sensitive to terrestrial input (Varma et al., 2025). RI-OH' in the surface sediments varies
340 from 0.05 to 0.17 while TEX-OH varies from 0.08 to 0.32. Both indexes plot in the global calibration curves from
341 (Varma et al., 2024) and the reconstructed SST varies from 0.9 to $4.0 \text{ }^\circ\text{C}$ and -0.1 to $11.6 \text{ }^\circ\text{C}$, respectively. TEX-OH
342 reconstructed SSTs in PCB09 varied between $7 \pm 2.6 \text{ }^\circ\text{C}$ in the Early Holocene, remained stable during the **Mid-**
343 **Holocene** ($\sim 3 \pm 2.6 \text{ }^\circ\text{C}$), decreased to $0 \pm 2.6 \text{ }^\circ\text{C}$ between 1-1.5 ka and after which they increase to $5 \pm 2.6 \text{ }^\circ\text{C}$, close to
344 modern summer SST (Locarnini et al., 2024). The reconstructed SST in the multicore is $-1 \pm 2.6 \text{ }^\circ\text{C}$, similar, within
345 the calibration error, to modern annual SST (Locarnini et al., 2024) (Fig. 4d). RI-OH' reconstructed SSTs in PCB09
346 produce high temperatures ($\sim 12 \pm 2.6 \text{ }^\circ\text{C}$) between 7 and 10 ka, maybe due to non-thermal impact on the production
347 of OH-GDGT (Harning & Sepúlveda, 2024). For both cores, reconstructed SST using RI-OH' is stable around $3 \text{ }^\circ\text{C}$
348 (Fig. S5b). PCB11 TEX-OH reconstructed SSTs are stable during the Early to **Mid-Holocene** ($\sim 5.0 \pm 2.6 \text{ }^\circ\text{C}$). However,
349 after 1 ka the reconstruction produces unrealistically large variation ($5\text{--}15 \text{ }^\circ\text{C}$, Fig. S5a).

350 The BIT index showed a steady decrease in PCB11 throughout the Holocene and until 3 ka in PCB09 (Fig. 4c). In
351 PCB09, this decrease was interrupted at 9 ka and at 1.5 ka with BIT index values reaching 0.3 and 0.4, respectively.
352 The increase at 9 ka was likely due to a relative decrease in crenarchaeol concentration (Fig. S5a) whereas the 1.5 ka
353 increase was likely due to a decrease in brGDGT concentration (Fig. 4i).



354

355 Figure 4: Reconstructed environmental parameters for PCB09 (brown circles) and PCB11 (red squares) (a) $P_{III}IP_{25}$
 356 (PIP₂₅ calculated with HBI III as phytoplankton biomarker), (b) $\delta^{2\text{H}}$ of $\text{C}_{16:0}$ fatty acid and corresponding reconstructed
 357 salinity (Sachs et al., 2018), (c) BIT index (Hopmans et al., 2004), (d) SST derived from TEX-OH (Varma et al., 2024)
 358 shaded areas indicate the uncertainties of the reconstruction, modern (1995-2004) annual and summer SSTs were
 359 extracted from (Locarnini et al., 2024) (e), global sea level estimates derived from Lambeck et al., (2014) and (f) 21
 360 June insolation at 70°N (Laskar et al., 2004). Panel g) Illustrative examples of paleoshorelines at 8 and 4 ka compared
 361 to the modern. These were generated by adjusting the sea-level using the modern bathymetry portrayed in IBCAO V.
 362 5 (Jakobsson et al., 2024). Relative sea-level adjustments were taken from ICE 6G_C (Peltier et al., 2015) for the grid
 363 cell encompassing the position of PCB11. The sea-level adjustments for this location were 46 m at 8 ka and 12 m at
 364 4 ka (Figure S7).

365

366 3.6. Micropaleontology

367 Almost all of the planktonic foraminifera (99-100% in abundance relative to other species) observed in PCB09 are *N.*
 368 *pachyderma*, formerly *N. pachyderma sinistra*. This is expected since this species has been found to dominate polar

369 water masses (e.g. Eynaud 2011; Moller, Schulz, and Kucera 2013). Planktonic foraminifera are mostly absent in
370 PCB11, consistent with data from plankton tows indicating that planktic foraminifera are rare on the Canadian shelf
371 where surface waters are influenced by Mackenzie River discharge (Vilks, 1989). In PCB09, the foraminiferal shells
372 appear white and fragmented in sections with abundant light-colored and sand-sized ice-rafted debris and other detrital
373 materials (Fig. S6). Foraminifera are more abundant in samples that have relatively more mud aggregates than sand-
374 sized debris (Fig. 2a,b). There is almost zero accumulation rate (per mm yr⁻¹) of *N. pachyderma* within the shelf slope
375 from 10 ka.

376 **4. Discussion**

377 This study aims to reconstruct Holocene paleoenvironmental conditions in the southeastern Beaufort Sea focusing on
378 spatial variability between the shelf slope (> 500m water depth) and the outer shelf (<100 m water depth). By analyzing
379 the abundance and ratios of sea ice biomarkers (IP₂₅, HBI II), phytoplankton and heterotrophic archaeal productivity
380 markers (HBI III, HBI IV, iso- and OH-GDGT), terrestrial inputs (brGDGTs, terrestrial sterols), and reconstructed
381 environmental indicators (salinity, SST) this study aim to highlight spatial environmental difference between a shallow
382 (PCB11) and deep (PCB09) site. In the following sections, we interpret biomarker records in a chronological
383 framework, highlighting the dynamic relationship between freshwater inputs, ocean circulation, and sea ice conditions.

384 **4.1. Late glacial to Early Holocene (12 – 8.2 ka)**

385 The **Late glacial** to Early Holocene is only recorded at the shelf slope location (PCB09, Fig. 1). This period is
386 characterized by low concentrations of sea ice biomarkers (Fig. 3a,b) resulting in low PIP₂₅ values (Fig. 4a). The low
387 concentration suggests that this area had intermittent sea ice coverage during the **Late glacial** to Early Holocene, but
388 the presence of HBI III and HBI IV (Fig. 3e,f) indicate that the region was only under seasonal ice cover until spring
389 allowing late spring/summer open-water diatom primary production (Belt et al., 2015). Heterotrophic production in
390 the shelf slope region during this period is relatively low (as suggested by the presence of ammonium oxidizer
391 Thaumarchaea-derived isoGDGTs, Schouten et al., 2013, Fig. 3g, h) but increased and peaked at 8.2 ± 0.5 ka. During
392 12 – 8.2 ka, SSTs were elevated in comparison with the rest of the Holocene (Fig. 4d) which coincided with peak 21
393 June insolation (Fig. 4f) (Clemens et al., 2010; Laskar et al., 2004). The warmer surface waters might have inhibited
394 the development of sea ice over the Beaufort Shelf.

395 During the Late glacial to Early Holocene, large freshwater inputs to the Beaufort Shelf, inferred from the low
396 reconstructed salinity (Fig. 4b) likely originated from the decaying Laurentide Ice Sheet. Such water masses derived
397 from drainage regions that had undergone minimal weathering would have released low amounts of nutrients. The
398 influx of low-salinity freshwater may have intensified salinity-driven stratification on the shelf, reducing the upwelling
399 of nutrient-rich saline Pacific waters to the surface which also limited nutrient availability. This stratification and
400 lower nutrient availability likely limited primary productivity and the presence of ammonia-oxidizers on the Beaufort
401 Shelf. It is important to note that sea level on the Beaufort Shelf was >60 m lower in the Early Holocene than it is
402 today (Fig. 4e). Implying that between 10-12 ka, the Beaufort Sea was a shallow estuarine environment (Fig. 4g, Hill
403 et al., 1993).

404 The concentration of brGDGTs and terrestrial sterols in the shelf slope location during the Early Holocene peaked at
405 11.3 ± 0.3 and 8.2 ± 0.5 ka (Fig. 3i,j), which agrees with meltwater outflow from the LIS and freshly deglaciated
406 surfaces as seen in nearby cores (Klotsko et al., 2019; J. Wu et al., 2020). Additionally, increased freshwater input
407 may have transported more detrital calcium (Ca), as indicated by elevated Ca/Ti ratios (Fig. 2a), which could have
408 enhanced the preservation of foraminifera by buffering the water column and limiting carbonate dissolution, in
409 sediments along the shelf slope. Murton et al. (2010) used optically stimulated luminescence (OSL) dating to identify
410 two major meltwater pulses through the Mackenzie River system between 13 and 11.7 ka and between 11.7 and 9.3
411 ka. This timing is supported by sedimentary and isotopic records from the Beaufort Sea indicating a major Lake
412 Agassiz flood route through the Mackenzie system (Keigwin et al., 2018; Klotksko et al., 2019). These meltwater events
413 coincide with events (11.3 ± 0.3 , 8.2 ± 0.5 ka) in the biomarker records from this study (Fig. 3), and one event at 10.1 ± 0.4 ka is recorded in the reconstructed salinity (Fig. 4b), suggesting enhanced freshwater forcing impacted ocean
415 circulation and increased sea ice extent. The massive meltwater discharge from the LIS (at least ~ 9000 km³) into its
416 surrounding oceans has been the major cause for eustatic sea level rise from 10 to 6 ka (Moran & Bryson, 1969).

417 **4.2. Middle to Late Holocene (8.2 – 0 ka)**

418 After 8.2 ka, environmental conditions at the shelf slope (PCB09) and the outer shelf (PCB11) diverged markedly,
419 reflecting their contrasting depositional and oceanographic settings. At PCB09, SSTs cooled from ~ 6 °C to 3 °C (Fig.
420 4d), while steadily increasing sea-ice biomarker concentrations led to $\text{PIP}_{25} > 0.5$ by 7-6 ka, indicating the

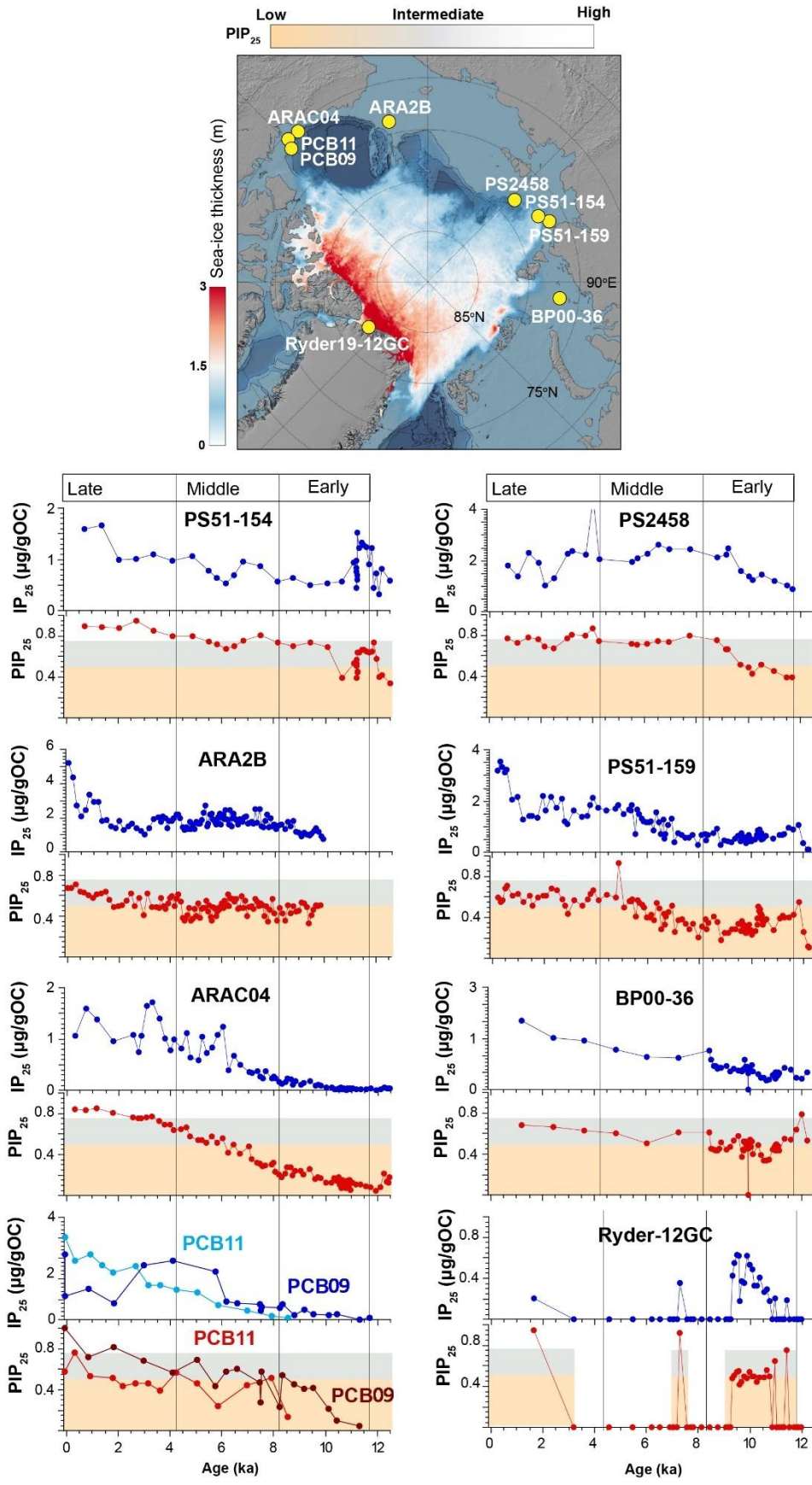
421 establishment of stable ice-edge or polynya conditions at the slope. The higher salinity (Fig. 4b) and greater distance
422 from the coast at this site suggest enhanced influence of offshore Pacific-derived waters and reduced terrestrial input.

423 In contrast, at the outer shelf site PCB11, sea-ice biomarkers also increased after 8.5 ka but were accompanied by
424 persistently high concentrations of open-water diatom markers, implying continued seasonal sea-ice and productive
425 flaw-lead conditions, i.e., an open-water or newly formed sea-ice zone between landfast ice and sea ice. The flaw-lead
426 today occurs about 80 km away from shore (Fig. S1) (Carmack et al., 2004). The proximity of PCB11 to the coastline
427 before 6 ka (Fig. 4g) likely favored landfast-ice diatom assemblages and greater sensitivity to freshwater discharge.
428 Only after 4 ± 0.5 ka did PCB11 reach PIP_{25} values comparable to the slope, indicating a delayed transition to stable
429 seasonal sea ice, approximately 2 kyr later than at PCB09. Thus, while both sites record a Middle-Holocene trend
430 toward increasing sea-ice cover, the slope experienced earlier stabilization and reduced productivity linked to offshore
431 cooling and stratification, whereas the outer shelf remained a dynamic, seasonally open-water environment likely
432 sustained by coastal flaw-lead formation, and strong riverine influence.

433 In the Late Holocene (4.2 ka to present), the two Beaufort sites again show distinct sea-ice and productivity trajectories
434 reflecting their different hydrographic settings. At the slope site, perennial sea ice cover developed after 3 ka as
435 indicated by higher PIP_{25} values (>0.8), increased reconstructed salinity (Fig. 4a,b), as well as a decline in open-water
436 diatom biomarkers (Fig. 3e,f). A sharp decrease in PIP_{25} and open-water diatom biomarkers at 1.5 ± 1.5 ka suggests a
437 shift to year-round ice cover coincident with low SST (~ 0 °C, Fig. 4d). The parallel reduction in heterotrophic archaeal
438 production may reflect strengthened water-column stratification or reduced nutrient supply, consistent with restricted
439 shelf-break upwelling (Schulze & Pickart, 2012). These changes are broadly consistent with the timing of the regional
440 cooling associated with the Little Ice Age (Mann et al., 2009), although the resolution of the biomarker record does
441 not allow precise attribution to centennial-scale events. In contrast, on the outer shelf, seasonal sea-ice conditions
442 persisted longer and sea ice cover expanded gradually and became well established after about 2 ± 0.6 ka. Even as
443 sea-ice biomarkers increased, open-water diatom markers remained relatively abundant, implying continued flaw-lead
444 or marginal-ice-zone productivity sustained by intermittent open-water formation and coastal influence.

445 By the last 0.4 ka, both sites reached modern configurations, but with clear spatial differences: PCB09 records
446 persistently thick, multi-year ice and limited primary production, whereas PCB11 retains higher concentrations of

447 both sea-ice and open-water diatom biomarkers, consistent with modern flaw-lead dynamics observed near the outer



449 Figure 5: Arctic sea-ice records (PIP₂₅ and IP₂₅ concentration) covering the Holocene: PCB (this study), ARAC04 (*J.*
450 *Wu et al.*, 2020), ARA2B (Stein et al., 2017), PS51-154 and PS51-159 (Hörner et al., 2016), PS5428 (Fahl & Stein,
451 2012), BP0036 (Hörner et al., 2018), Ryder19-12 (Detlef et al., 2023). Average thickness of sea ice (in meters) for
452 September 2023. Data from the Arctic Ocean Sea Ice Reanalysis (Williams et al., 2021) obtained via the E.U.
453 Copernicus Marine Service Information MyOcean Viewer (<https://marine.copernicus.eu/access-data/myocean-viewer>). The shaded rectangles indicate the limit of the proxy for no sea-ice in red, seasonal sea ice in blue
454 (0.5 < PIP₂₅ < 0.75) and permanent sea ice above PIP₂₅ > 0.75.

456 **4.3. Comparison with other Arctic marginal seas**

457 Previous studies using IP₂₅ to reconstruct sea ice variability in Arctic marginal seas have reported largely open-water
458 conditions with significant freshwater influence during the **Late glacial** to Early Holocene.

459 The nearby cores JPC15 (Keigwin et al., 2018), ARAC20 (J. Wu et al., 2020) (Fig. 1) recorded similar environmental
460 changes (sea ice cover, freshwater input) as in PCB09 but different from those recorded in the shallow PCB11 site,
461 highlighting the differences between shelf slope and outer shelf and the spatial variation of the polynya position. Aside
462 from the close-by cores (Keigwin et al., 2018; Klotsko et al., 2019; J. Wu et al., 2020), other Arctic records in the
463 Canadian Archipelago (Vare et al., 2009), East Siberian (Dong et al., 2022), Kara (Hörner et al., 2018) , Chukchi
464 (Stein et al., 2017), Laptev (Fahl & Stein, 2012; Hörner et al., 2016), and Lincoln (Detlef et al., 2023) Seas and along
465 the Lomonosov Ridge (Stein & Fahl, 2012), report minimum sea-ice cover during the Early Holocene (centered around
466 10 ka) (Fig. 5). Detlef et al. (2023) reconstructed sea ice conditions from a sediment core covering the last 11 ka,
467 showing that while the Lincoln Sea currently experiences perennial sea ice cover (PIP₂₅ = 0), it underwent a shift to
468 seasonal sea ice during the Early Holocene (around 10 ka) due to significantly warmer conditions (PIP₂₅ > 0.5). This
469 period of reduced sea ice cover is associated with increased marine productivity and meltwater input indicated by
470 biomarker and sedimentary facies. The Northern Greenland (Detlef et al., 2023) and the site offshore the Laptev Sea
471 on the Lomonosov Ridge (Fahl & Stein, 2012; Hörner et al., 2016) are the first regions to record permanent sea-ice
472 cover beginning around 9 ka after the Early Holocene minimum. The Beaufort Sea (this study, J. Wu et al., 2020)
473 showed permanent sea-ice cover over the slope after 3 ka. Seasonal sea-ice cover in the shallower regions of the
474 Laptev and Beaufort Seas (PS51-159 and PCB11) was developed after 5 and 3 ka, respectively. The Chukchi Sea
475 (ARA2B) had seasonal sea-ice from the **Mid-Holocene** onwards, with an increase after 4.5 ka (Stein et al., 2017). The
476 variations in sea ice cover and primary production in the Chukchi Sea were attributed to differences in solar insolation
477 and variability in Pacific water inflow, which brought increased heat flux and episodic declines in sea ice cover. In
478 the Canadian Archipelago, a record that did not include the Early Holocene, (Belt et al., 2010; Vare et al., 2009)
479 increased sea-ice cover exists from 7 to 3 ka.

480 In contrast, studies using dinocyst assemblages from around the Arctic Ocean (see the review of de Vernal et al., 2013)
481 report constant sea ice cover for the Early to **Mid-Holocene** with a clear decrease around 6 ka, followed by a return to
482 pre-6 ka conditions until an increase toward modern times. This could be due to a warm-bias in the dinocyst estimate
483 or a non-representative training set (de Vernal et al., 2013).

484 Together, many of the biomarker studies provide a consistent narrative of spring sea ice development during the
485 Holocene across the Arctic Ocean following a period of high insolation in the Early Holocene. The transition from
486 largely open-water and freshwater-influenced conditions during the **Late glacial** to Early Holocene to increasing sea
487 ice cover from the **Mid-Holocene** onward is a shared feature across the Arctic shelf seas, although regional variations
488 in sea ice dynamics and productivity are observed due to local freshwater input and oceanographic conditions.
489 Evidence from areas with permanent sea ice, such as the Lincoln Sea, shows that the minimum ice cover during the
490 **Late glacial** extended even into the high Arctic, offering insights into the extent of sea ice reduction during this time.

491 **5. Conclusions**

492 Analysis of two sediment cores from the outer Beaufort Shelf and shelf slope help elucidate the region's
493 paleoenvironmental variability throughout the Holocene. The shelf slope experienced ice-free to minimal sea ice
494 extent during the **Late glacial** and Early Holocene. During the Early Holocene, the Beaufort Shelf was ~60 m shallower
495 than today, and experienced large freshwater influxes due to the decaying LIS. The following sea level rise brought
496 the core sites further away from the river mouth and eroding permafrost coasts, lowering the input of terrestrial organic
497 matter. Cooling during the **Mid-Holocene** drove an increase in sea ice cover for the Beaufort Shelf and other Arctic
498 marginal seas. Sea-ice cover and its impact on local upwelling and regional Pacific inflow impacted local primary
499 production, concentrating the phytoplankton production in open-water flaw-lead or polynya conditions. Open water
500 conditions substantially decreased during the Late Holocene as extended sea ice cover developed at the shelf slope,
501 which caused primary productivity to further decline. This study highlights broadly consistent patterns of sea ice
502 variability across Arctic marginal seas, implying similar controls on sea-ice dynamics, and underscoring the
503 vulnerability of perennial sea-ice as contemporary climate conditions reach or surpass those from the Early Holocene.

504 **Data availability**

505 The research data are published on the Bolin Center database 10.17043/lattaud-2025-sediment-beaufort-surface-1 and
506 10.17043/lattaud-2025-sediment-beaufort-1.

507 **Author contribution** MS - Data Curation, Formal analysis, Investigation, Writing – original draft preparation, LBr
508 Conceptualization, Supervision, Funding acquisition, Writing – review & editing, MO Resource, Funding acquisition,
509 Investigation, Writing – review & editing IH Conceptualization, Supervision, Writing – review & editing, TT
510 Resource, Writing – review & editing LBi Investigation, NH Resource, Writing – review & editing, DN Resource,
511 Writing – review & editing, MF Funding acquisition, Writing – review & editing, JL Conceptualization, Funding
512 acquisition, Investigation, Project administration, Supervision, Writing – review & editing

513 **Competing interest** The authors declare that they have no conflict of interest.

514 **Acknowledgments**

515 We thank Amundsen Science and ArcticNet for their support in preparing the cruise and the crew of the CCGS
516 Amundsen and the PeCaBeau team for their help during sampling. We thank the Alfred Wegener Institute for
517 providing the multicorer and part of the logistical support. Carina Johansson is thanked for her help with XRF analysis,
518 and Axel Birkholz and Thomas Kuhn for the bulk elemental and isotopic analysis. MS was funded through a SNSF-
519 Ambizione (PZ00P2-209012) to JL. The ship-time leading to sample acquisition for this study was funded by the
520 European Union H2020 as part of the EU Project ARICE (grant agreement n° 730965) with additional support from
521 the Swiss Polar Institute (Project number PAF-2020-004).

522

523 **References**

524 Belt, Simon T., Guillaume Massé, Steven J. Rowland, Michel Poulin, Christine Michel, and Bernard LeBlanc. 2007.

525 “A Novel Chemical Fossil of Palaeo Sea Ice: IP₂₅.” *Organic Geochemistry* 38 (January): 16–27.

526 <https://doi.org/10.1016/j.orggeochem.2006.09.013>.

527 Belt, Simon T., and Juliane Müller. 2013. “The Arctic Sea Ice Biomarker IP₂₅: A Review of Current Understanding, Recommendations for Future Research and Applications in Palaeo Sea Ice Reconstructions.” *Quaternary Science Reviews* 79 (November): 9–25. <https://doi.org/10.1016/j.quascirev.2012.12.001>.

530 Broecker, Wallace S., James P. Kennett, Benjamin P. Flower, James T. Teller, Sue Trumbore, Georges Bonani, and
531 Willy Wolfli. 1989. “Routing of Meltwater from the Laurentide Ice Sheet During the Younger Dryas Cold Episode.”
532 *Nature* 341 (September): 318–21. <https://doi.org/10.1038/341318a0>.

533 Brown, T. A., S. T. Belt, A. Tatarek, and C. J. Mundy. 2014. “Source Identification of the Arctic Sea Ice Proxy IP₂₅.”
534 *Nature Communications* 5 (June): 4197. <https://doi.org/10.1038/ncomms5197>.

535 Buizert, Christo, Vasileios Gkinis, Jeffrey P. Severinghaus, Feng He, Benoit S. Lecavalier, Philippe Kindler, Markus
536 Leuenberger, et al. 2014. “Greenland Temperature Response to Climate Forcing During the Last Deglaciation.”
537 *Science* 345 (September): 1177–80. <https://doi.org/10.1126/science.1254961>.

538 Carlson, Anders E., Allegra N. LeGrande, Delia W. Oppo, Rosemarie E. Came, Gavin A. Schmidt, Faron S. Anslow,
539 Joseph M. Licciardi, and Elizabeth A. Obbink. 2008. “Rapid Early Holocene Deglaciation of the Laurentide Ice
540 Sheet.” *Nature Geoscience* 1 (9): 620–24. <https://doi.org/10.1038/ngeo285>.

541 Carmack, EC, RW Macdonald, and S Jasper. 2004. “Phytoplankton Productivity on the Canadian Shelf of the Beaufort
542 Sea.” *Marine Ecology Progress Series* 277: 37–50. <https://doi.org/10.3354/meps277037>.

543 Dai, Aiguo, Dehai Luo, Mirong Song, and Jiping Liu. 2019. “Arctic Amplification Is Caused by Sea-Ice Loss Under
544 Increasing CO₂.” *Nature Communications* 10 (January): 121. <https://doi.org/10.1038/s41467-018-07954-9>.

545 Data, I. E. 2021) National Snow and Ice Data Center. <https://nsidc.org/>

546 Detlef, Henrieka, Matt O'Regan, Christian Stranne, Mads Mørk Jensen, Marianne Glasius, Thomas M. Cronin, Martin
547 Jakobsson, and Christof Pearce. 2023. "Seasonal Sea-Ice in the Arctic's Last Ice Area During the Early Holocene."
548 *Communications Earth & Environment* 4 (1). <https://doi.org/10.1038/s43247-023-00720-w>.

549 Eicher, O.; Baumgartner, M.; Schilt, A.; Schmitt, J.; Schwander, J.; Stocker, T.F.; Fischer, H. (2016-10-06):
550 NOAA/WDS Paleoclimatology - NGRIP Ice Core 120,000 Year Total Air Content Data. [indicate subset used].
551 NOAA National Centers for Environmental Information. <https://doi.org/10.25921/n0d0-ng26>. Accessed [July 2023].

552 Eynaud, Frédérique. 2011. "Planktonic Foraminifera in the Arctic: Potentials and Issues Regarding Modern and
553 Quaternary Populations." *IOP Conference Series: Earth and Environmental Science* 14 (May): 012005.
554 <https://doi.org/10.1088/1755-1315/14/1/012005>.

555 Fietz, Susanne, Sze Ling Ho, and Carme Huguet. 2020. "Archaeal Membrane Lipid-Based Paleothermometry for
556 Applications in Polar Oceans." *Oceanography* 33 (June). <https://doi.org/10.5670/oceanog.2020.207>.

557 Frey, K. E., J. C. Comiso, L. W. Cooper, J. M. Grebmeier, and L. V. Stock. 2020. "Arctic Ocean Primary Productivity:
558 The Response of Marine Algae to Climate Warming and Sea Ice Decline - NOAA Arctic — Arctic.noaa.gov."
559 <https://arctic.noaa.gov/Report-Card/Report-Card-2020/ArtMID/7975/ArticleID/900/Arctic-Ocean-Primary->
560 Productivity-The-Response-of-Marine-Algae-to-Climate-Warming-and-Sea-Ice-Decline.

561 Häkkinen, Sirpa. 1987. "Upwelling at the Ice Edge: A Mechanism for Deep Water Formation?" *Journal of*
562 *Geophysical Research* 92 (C5): 5031. <https://doi.org/10.1029/jc092ic05p05031>.

563 Hartman, Julian D., F. Sangiorgi, M. A. Barcena, F. Tateo, F. Giglio, S. Albertazzi, F. Trincardi, P. K. Bijl, L. Langone,
564 and A. Asioli. 2021. "Sea-Ice, Primary Productivity and Ocean Temperatures at the Antarctic Marginal Zone During
565 Late Pleistocene." *Quaternary Science Reviews* 266 (August): 107069.
566 <https://doi.org/10.1016/j.quascirev.2021.107069>.

567 Herfort, Lydie, Stefan Schouten, Ben Abbas, Marcel J. W. Veldhuis, Marco J. L. Coolen, Cornelia Wuchter, Jan P.
568 Boon, Gerhard J. Herndl, and Jaap S. Sinninghe Damste. 2007. "Variations in Spatial and Temporal Distribution of
569 Archaea in the North Sea in Relation to Environmental Variables." *FEMS Microbiology Ecology* 62 (3): 242–57.
570 <https://doi.org/10.1111/j.1574-6941.2007.00397.x>.

571 Hill, Philip R., Arnaud Héquette, and Marie-Hélène Ruz. 1993. "Holocene Sea-Level History of the Canadian Beaufort
572 Shelf." *Canadian Journal of Earth Sciences* 30 (1): 103–8. <https://doi.org/10.1139/e93-009>.

573 Huguet, C., Kim, J., Sininghe Damsté, J. S., and Schouten, S. 2006: Reconstruction of sea surface temperature
574 variations in the Arabian Sea over the last 23 kyr using organic proxies (TEX86 and U37K'), *Paleoceanography*, 21,
575 <https://doi.org/10.1029/2005pa001215>.

576 Hopmans, Ellen C, Johan W. H Weijers, Enno Schefuß, Lydie Herfort, Jaap S Sininghe Damsté, and Stefan Schouten.
577 2004. "A Novel Proxy for Terrestrial Organic Matter in Sediments Based on Branched and Isoprenoid Tetraether
578 Lipids." *Earth and Planetary Science Letters* 224 (July): 107–16. <https://doi.org/10.1016/j.epsl.2004.05.012>.

579 Kashiwase, Haruhiko, Kay I. Ohshima, Sohey Nihashi, and Hajo Eicken. 2017. "Evidence for Ice-Ocean Albedo
580 Feedback in the Arctic Ocean Shifting to a Seasonal Ice Zone." *Scientific Reports* 7 (August): 8170.
581 <https://doi.org/10.1038/s41598-017-08467-z>.

582 Keigwin, L. D., S. Klotisko, N. Zhao, B. Reilly, L. Giosan, and N. W. Driscoll. 2018. "Deglacial Floods in the Beaufort
583 Sea Preceded Younger Dryas Cooling." *Nature Geoscience* 11 (8): 599–604. [https://doi.org/10.1038/s41561-018-0169-6](https://doi.org/10.1038/s41561-018-
584 0169-6).

585 Lake, Robert Alan. 1967. "Heat Exchange Between Water and Ice in the Arctic Ocean." *Archiv Für Meteorologie,
586 Geophysik Und Bioklimatologie Serie A* 16 (October): 242–59. <https://doi.org/10.1007/BF02246401>.

587 Laskar, J., P. Robutel, F. Joutel, M. Gastineau, A. C. M. Correia, and B. Levrard. 2004. "A Long-Term Numerical
588 Solution for the Insolation Quantities of the Earth." *Astronomy & Astrophysics* 428 (December): 261–85.
589 <https://doi.org/10.1051/0004-6361:20041335>.

590 Lattaud, J., Bröder, L., Haghipour, N., Rickli, J., Giosan, L., and Eglinton, T. I. 2021. Influence of Hydraulic
591 Connectivity on Carbon Burial Efficiency in Mackenzie Delta Lake Sediments, *Journal of Geophysical Research:
592 Biogeosciences*, 126. <https://doi.org/10.1029/2020jg006054>.

593 Leri, A. C., Mayer, L. M., Thornton, K. R., and Ravel, B. 2014. Bromination of marine particulate organic matter
594 through oxidative mechanisms, *Geochimica et Cosmochimica Acta*, 142, 53–63,
595 <https://doi.org/10.1016/j.gca.2014.08.012>.

596 Liu, Xiao-Lei, Julius S. Lipp, Jeffrey H. Simpson, Yu-Shih Lin, Roger E. Summons, and Kai-Uwe Hinrichs. 2012.
597 “Mono- and Dihydroxyl Glycerol Dibiphytanyl Glycerol Tetraethers in Marine Sediments: Identification of Both Core
598 and Intact Polar Lipid Forms.” *Geochimica Et Cosmochimica Acta* 89 (July): 102–15.
599 <https://doi.org/10.1016/j.gca.2012.04.053>.

600 Lü, Jun-Mei, Seong-Joong Kim, Ayako Abe-Ouchi, Yongqiang Yu, and Rumi Ohgaito. 2010. “Arctic Oscillation
601 During the Mid-Holocene and Last Glacial Maximum from PMIP2 Coupled Model Simulations.” *Journal of Climate*
602 23 (14): 3792–3813. <https://doi.org/10.1175/2010jcli3331.1>.

603 Lü, Xiaoxia, Xiao-Lei Liu, Felix J. Elling, Huan Yang, Shucheng Xie, Jinming Song, Xuegang Li, Huamao Yuan,
604 Ning Li, and Kai-Uwe Hinrichs. 2015. “Hydroxylated Isoprenoid GDGTs in Chinese Coastal Seas and Their Potential
605 as a Paleotemperature Proxy for Mid-to-Low Latitude Marginal Seas.” *Organic Geochemistry* 89–90 (December): 31–
606 43. <https://doi.org/10.1016/j.orggeochem.2015.10.004>.

607 Marcott, Shaun A., Jeremy D. Shakun, Peter U. Clark, and Alan C. Mix. 2013. “A Reconstruction of Regional and
608 Global Temperature for the Past 11,300 Years.” *Science* 339 (March): 1198–1201.
609 <https://doi.org/10.1126/science.1228026>.

610 Matero, I. S. O., L. J. Gregoire, R. F. Ivanovic, J. C. Tindall, and A. M. Haywood. 2017. “The 8.2 Ka Cooling Event
611 Caused by Laurentide Ice Saddle Collapse.” *Earth and Planetary Science Letters* 473 (September): 205–14.
612 <https://doi.org/10.1016/j.epsl.2017.06.011>.

613 McNichol, A. P., E. A. Osborne, A. R. Gagnon, B. Fry, and G. A. Jones. 1994. “TIC, TOC, DIC, DOC, PIC, POC —
614 Unique Aspects in the Preparation of Oceanographic Samples for 14C-AMS.” *Nuclear Instruments and Methods in
615 Physics Research Section B: Beam Interactions with Materials and Atoms* 92 (1–4): 162–65.
616 [https://doi.org/10.1016/0168-583x\(94\)95998-6](https://doi.org/10.1016/0168-583x(94)95998-6).

617 Moller, Tobias, Hartmut Schulz, and Michal Kucera. 2013. “The Effect of Sea Surface Properties on Shell Morphology
618 and Size of the Planktonic Foraminifer *Neogloboquadrina pachyderma* in the North Atlantic.” *Palaeogeography,
619 Palaeoclimatology, Palaeoecology* 391 (December): 34–48. <https://doi.org/10.1016/j.palaeo.2011.08.014>.

620 Moran, Joseph M., and Reid A. Bryson. 1969. "The Contribution of Laurentide Ice Wastage to the Eustatic Rise of
621 Sea Level: 10, 000 to 6, 000 BP." *Arctic and Alpine Research* 1 (2): 97. <https://doi.org/10.2307/1550016>.

622 Müller, Juliane, Kirstin Werner, Ruediger Stein, Kirsten Fahl, Matthias Moros, and Eystein Jansen. 2012. "Holocene
623 Cooling Culminates in Sea Ice Oscillations in Fram Strait." *Quaternary Science Reviews* 47 (July): 1–14.
624 <https://doi.org/10.1016/j.quascirev.2012.04.024>.

625 Murton, Julian B., Mark D. Bateman, Scott R. Dallimore, James T. Teller, and Zhirong Yang. 2010. "Identification
626 of Younger Dryas Outburst Flood Path from Lake Agassiz to the Arctic Ocean." *Nature* 464 (7289): 740–43.
627 <https://doi.org/10.1038/nature08954>.

628 NGRIP-Members. 2004. "High-Resolution Record of Northern Hemisphere Climate Extending into the Last
629 Interglacial Period." *Nature* 431 (7005): 147–51. <https://doi.org/10.1038/nature02805>.

630 Not, Christelle, and Claude Hillaire-Marcel. 2012. "Enhanced Sea-Ice Export from the Arctic During the Younger
631 Dryas." *Nature Communications* 3 (January): 647. <https://doi.org/10.1038/ncomms1658>.

632 Omstedt, Anders, Eddy C. Carmack, and Robie W. Macdonald. 1994. "Modeling the Seasonal Cycle of Salinity in
633 the Mackenzie Shelf/Estuary." *Journal of Geophysical Research* 99: 10011. <https://doi.org/10.1029/94JC00201>.

634 Park, Hyo-Seok, Seong-Joong Kim, Andrew L. Stewart, Seok-Woo Son, and Kyong-Hwan Seo. 2019. "Mid-Holocene
635 Northern Hemisphere Warming Driven by Arctic Amplification." *Science Advances* 5 (12).
636 <https://doi.org/10.1126/sciadv.aax8203>.

637 Pfalz, Gregor, Bernhard Diekmann, Johann-Christoph Freytag, Liudmila Syrykh, Dmitry A. Subetto, and Boris K.
638 Biskaborn. 2022. "Improving Age–Depth Relationships by Using the LANDO ('Linked Age and Depth Modeling')
639 Model Ensemble." *Geochronology* 4 (1): 269–95. <https://doi.org/10.5194/gchron-4-269-2022>.

640 Pickart, Robert S. 2004. "Shelfbreak Circulation in the Alaskan Beaufort Sea: Mean Structure and Variability."
641 *Journal of Geophysical Research* 109: C04024. <https://doi.org/10.1029/2003JC001912>.

642 Rantanen, Mika, Alexey Yu. Karpechko, Antti Lipponen, Kalle Nordling, Otto Hyvärinen, Kimmo Ruosteenoja, Timo
643 Vihma, and Ari Laaksonen. 2022. “The Arctic Has Warmed Nearly Four Times Faster Than the Globe Since.”
644 *Communications Earth & Environment* 3 (August): 168. <https://doi.org/10.1038/s43247-022-00498-3>.

645 Richter, T. O., Gaast, S. van der, Koster, B., Vaars, A., Gieles, R., Stigter, H. C. de, Haas, H. De and Weering, T. C.E.
646 van. 2005. The Avaatech XRF Core Scanner: technical description and applications to NE Atlantic sediments, Geol
647 Soc. London, Spec. Publ., 267(1), 39–50, doi:10.1144/GSL.SP.2006.267.01.03.

648 Sachs, J. P., Stein, R., Maloney, A. E., Wolhowe, M., Fahl, K., and Nam, S.-i. 2018. An Arctic Ocean paleosalinity
649 proxy from $\delta^{2}H$ of palmitic acid provides evidence for deglacial Mackenzie River flood events, *Quaternary Science*
650 *Reviews*, 198, 76–90, <https://doi.org/10.1016/j.quascirev.2018.08.025>.

651 Schouten, Stefan, Ellen C. Hopmans, and Jaap S. Sinninghe Damsté. 2013. “The Organic Geochemistry of Glycerol
652 Dialkyl Glycerol Tetraether Lipids: A Review.” *Organic Geochemistry* 54 (January): 19–61.
653 <https://doi.org/10.1016/j.orggeochem.2012.09.006>.

654 Schouten, Stefan, Ellen C. Hopmans, Enno Schefuß, and Jaap S. Sinninghe Damsté. 2002. “Distributional Variations
655 in Marine Crenarchaeotal Membrane Lipids: A New Tool for Reconstructing Ancient Sea Water Temperatures?”
656 *Earth and Planetary Science Letters* 204 (November): 265–74. [https://doi.org/10.1016/S0012-821X\(02\)00979-2](https://doi.org/10.1016/S0012-821X(02)00979-2).

657 Serreze, Mark C., and Jennifer A. Francis. 2006. “The Arctic Amplification Debate.” *Climatic Change* 76 (June):
658 241–64. <https://doi.org/10.1007/s10584-005-9017-y>.

659 Sinninghe Damsté, Jaap S., W. Irene C. Rijpstra, Marco J. L. Coolen, Stefan Schouten, and John K. Volkman. 2007.
660 “Rapid Sulfurisation of Highly Branched Isoprenoid (HBI) Alkenes in Sulfidic Holocene Sediments from Ellis Fjord,
661 Antarctica.” *Organic Geochemistry* 38 (1): 128–39. <https://doi.org/10.1016/j.orggeochem.2006.08.003>.

662 Smith, Richard W., Thomas S. Bianchi, and Xinxin Li. 2012. “A Re-Evaluation of the Use of Branched GDGTs as
663 Terrestrial Biomarkers: Implications for the BIT Index.” *Geochimica Et Cosmochimica Acta* 80 (March): 14–29.
664 <https://doi.org/10.1016/j.gca.2011.11.025>.

665 Steenfelt, A., Thomassen, B., Lind, M. and Kyed, J.: Karrat. 1998. reconnaissance mineral exploration in central West
666 Greenland, *Geol. Greenl. Surv. Bull.*, 180, 73–80.

667 Stein, Ruediger, Kirsten Fahl, Paul Gierz, Frank Niessen, and Gerrit Lohmann. 2017. "Arctic Ocean Sea Ice Cover
668 During the Penultimate Glacial and the Last Interglacial." *Nature Communications* 8 (August): 373.
669 <https://doi.org/10.1038/s41467-017-00552-1>.

670 Stein, Ruediger, and Robie W. MacDonald, eds. 2004. *The Organic Carbon Cycle in the Arctic Ocean*. Springer Berlin
671 Heidelberg. <https://doi.org/10.1007/978-3-642-18912-8>.

672 Stoll, Heather M., Isabel Cacho, Edward Gasson, Jakub Sliwinski, Oliver Kost, Ana Moreno, Miguel Iglesias, et al.
673 2022. "Rapid Northern Hemisphere Ice Sheet Melting During the Penultimate Deglaciation." *Nature Communications*
674 13: 3819. <https://doi.org/10.1038/s41467-022-31619-3>.

675 Teller, James T. 2013. "Lake Agassiz During the Younger Dryas." *Quaternary Research* 80: 361–69.
676 <https://doi.org/10.1016/j.yqres.2013.06.011>.

677 Ullman, David J., Anders E. Carlson, Steven W. Hostetler, Peter U. Clark, Joshua Cuzzone, Glenn A. Milne, Kelsey
678 Winsor, and Marc Caffee. 2016. "Final Laurentide Ice-Sheet Deglaciation and Holocene Climate-Sea Level Change."
679 *Quaternary Science Reviews* 152: 49–59. <https://doi.org/10.1016/j.quascirev.2016.09.014>.

680 Vernal, Anne de, Claude Hillaire-Marcel, Cynthia Le Duc, Philippe Roberge, Camille Brice, Jens Matthiessen, Robert
681 F. Spielhagen, and Ruediger Stein. 2020. "Natural Variability of the Arctic Ocean Sea Ice During the Present
682 Interglacial." *Proceedings of the National Academy of Sciences* 117: 26069–75.
683 <https://doi.org/10.1073/pnas.2008996117>.

684 Wu, Junjie, Ruediger Stein, Kirsten Fahl, Nicole Syring, Seung-II Nam, Jens Heft, Gesine Mollenhauer, and Walter
685 Geibert. 2020. "Deglacial to Holocene Variability in Surface Water Characteristics and Major Floods in the Beaufort
686 Sea." *Communications Earth & Environment* 1: 27. <https://doi.org/10.1038/s43247-020-00028-z>.